

# Efficient HDR Reconstruction From Real-World Raw Images

Qirui Yang<sup>1</sup>, Yihao Liu <sup>\*2</sup>, Qihua Chen<sup>3</sup>, and Jingyu Yang<sup>†1</sup>

<sup>1</sup>Electrical and Information Engineering, Tianjin University

<sup>2</sup>University of Chinese Academy of Sciences

<sup>3</sup>Shenzhen Bit Microelectronics Technology

## Abstract

High dynamic range (HDR) imaging is a significant yet challenging problem due to the limited dynamic range of generic image sensors. Most existing learning-based HDR reconstruction methods take a set of bracketed exposure sRGB images to extend the dynamic range. However, they overlook the computational and memory inefficiencies of Image Signal Processors (ISPs) when processing a set of sRGB images with different exposures. Furthermore, the absence of large-scale raw-based HDR datasets limits the research on HDR imaging. In this work, in a new aspect, we discover an excellent opportunity for HDR reconstructing directly from raw images and investigating novel neural network structures that benefit the deployment of mobile devices. Meanwhile, we construct a new HDR dataset containing raw images and process to obtain sRGB images and design a new model to reconstruct HDR utilizing the unique characteristics of long- and short-exposure images. Our key insights are threefold: (1) a new computational raw LDR-HDR pair formation pipeline is designed to construct a real-world raw HDR dataset called *RealRaw-HDR*; (2) a lightweight-efficient HDR model, *RePUNet*, is developed using the structural reparameterization technique; (3) a plug-and-play alignment-free and motion-aware short-exposure-first selection loss and a colorfulness loss are proposed to mitigate ghost artifacts and color cast. Extensive experiment results demonstrate that our approach achieves state-of-the-art performance in both visual quality and quantitative metrics.

## 1. Introduction

Most resource-constrained cameras exhibit low dynamic ranges (LDR), rendering them unable to capture the full

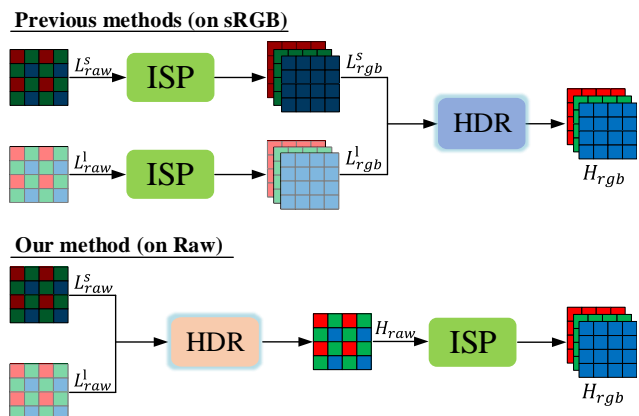


Figure 1. To address the HDR reconstruction problem, previous methods mainly focus on models trained on processed sRGB datasets, while we promote a novel view to address HDR reconstruction by training on raw images. Furthermore, compared with sRGB-based HDR reconstruction, raw-based HDR reconstruction is more beneficial and reduces the power consumption of ISP, DDR, and NPU by almost half.

range of brightness and color information in real-world scenes. Conversely, high dynamic range imaging seeks to encompass a significantly broader range of luminance values, compensating for color distortions and the subtle detail loss observed in LDR images. Despite the availability of dedicated hardware for directly acquiring HDR images, such equipment is typically expensive, thus limiting its practicality for most users. As a result, there has been an increasing focus on fusion-based HDR imaging methods tailored for LDR cameras.

Widely practiced HDR reconstruction methods [16, 5, 27, 37, 39] exploit a set of sRGB images with different exposure levels to produce an HDR image. However, capturing a set of bracketed exposure LDR images can be challenging, especially when the camera is shaking or there are moving objects in the viewfinder frame. [16]. In response

<sup>\*</sup>The first two authors are co-first authors

<sup>†</sup>Corresponding author, E-mail: yjy@tju.edu.cn

to this challenge, Sony has introduced a Digital Overlap (DOL) [41] HDR sensor and a Binned Multiplexed Exposure (BME) HDR sensor [24]. These sensors can shorten the time interval between different exposure images, enabling the “quasi-synchronous” capture of multiple raw images with different exposure times. Nonetheless, the quasi-synchronous mechanism retains relative motion between pre- and post-frames, which can introduce ghost artifacts in the reconstructed HDR results.

Although sRGB-based HDR reconstruction methods [38, 39] have made significant progress in recent years, these methods neglect three critical considerations. **Firstly**, as shown in Fig. 1, an ISP pipeline needs to be applied separately to different exposure LDR raw images to obtain different exposure LDR sRGB images, which are then reconstructed as an HDR image. The ISP pipeline typically involves complicated processes, including demosaicing, tone mapping, color and contrast tuning, denoising and sharpness, etc. These processes require significant memory and computational resources, which is very unfriendly to resource-limited sensors like security cameras. **Secondly**, existing approaches [16, 21] substitute the complex camera response curve with a simplistic inverse gamma function to obtain a set of pseudo-linear sRGB images with different exposures. However, this approach may produce non-luminance-aligned images in non-saturated regions during luminance alignment, thus rendering training more challenging. The linear characterization between the different exposure images of the raw images reduces the difficulty of luminance-aligned processing. **Thirdly**, the raw image data contains more detailed information, and the noise model is more straightforward. Meanwhile, the bit depth of the raw image is generally higher than that of the sRGB image, which is more beneficial to improving the dynamic range of the image. Therefore, the limitations inherent in the current sRGB-based HDR reconstruction methods highlight the necessity of further research and development in the domain of HDR imaging.

Building upon the above observations, we propose reconstructing HDR images from a set of raw LDR images with different exposures (as shown in Fig. 1). Accordingly, we introduce a novel raw LDR-HDR pair formation pipeline and obtain an associated training and testing dataset named RealRaw-HDR. In addition, we devise a simple yet effective raw HDR reconstruction network with reparameterization techniques, establishing a new baseline for the raw HDR reconstruction field. Specifically, upon exploring the HDR sensor imaging system, we discover that simulating the sensor’s Digital Gain can produce the same luminance level as altering the exposure time, given certain conditions. Leveraging this insight, we design a digital imaging pipeline that captures raw images with changing exposure gain based on the camera’s photoelectric signal

conversion model. By simulating the HDR sensor imaging system, we built a digital imaging pipeline to obtain raw images with different exposures, thus emerging as a practical tool for generating high-quality LDR-HDR images. The resultant RealRaw-HDR dataset encompasses a substantial collection of LDR-HDR pairs, serving as the foundation for training and evaluation. By incorporating the distinctive attributes of raw images into our approach, we can achieve elevated HDR reconstruction outcomes characterized by enhanced efficiency and accuracy.

To further advance the HDR imaging system, we introduce RepUNet, a lightweight and resource-efficient model for raw HDR reconstruction. RepUNet adopts reparameterization techniques, bypassing the need for computationally intensive alignment modules such as optical flow, deformation convolution, or attention mechanisms, which are commonly employed in existing deep learning-based HDR reconstruction methods [16, 21]. Furthermore, addressing the absence of explicit alignment modules, we introduce a plug-and-play alignment-free and motion-aware short-exposure-first selection loss (AMSS-Loss), which guides the network to focus on local motion regions, effectively mitigating ghost artifacts between short- and long-exposure images. This approach significantly reduces hardware expenses and enhances the real-time performance of HDR imaging systems.

Our contributions are summarized as follows:

- We propose a pioneering pipeline for forming LDR-HDR pairs based on sensor imaging theory, resulting in a large-scale, high-quality raw HDR dataset coined RealRaw-HDR. This dataset serves as the bedrock for follow-up raw HDR reconstruction methodologies.
- We develop a lightweight model, RepUNet, to achieve raw HDR reconstruction, which utilizes structural reparameterization techniques that notably curb the computational demands of hardware devices.
- We introduce a plug-and-play alignment-free and motion-aware short-exposure-first selection loss to mitigate ghost artifacts between short- and long-exposure images.

Our contributions signify a substantial advancement in raw HDR image reconstruction research, delivering an efficient and productive solution for producing superior HDR images. Extensive experiments demonstrate that our approach achieves state-of-the-art visual quality and quantitative metrics performance.

## 2. Related Work

### 2.1. HDR Imaging

The expansion of camera dynamic range has been a focal point of research over the past decades. One class of

technology [33, 31] involves achieving HDR image capture in a single shot by refining digital camera hardware design. The Dual Conversion Gain (DCG) sensor [15], for instance, enhances dynamic range through DCG circuitry, enabling image capture in extremely low-light conditions without compromising performance in high-light scenarios. Sun et al. [33] propose a method for single-exposure HDR imaging through end-to-end optical coding design. Regrettably, these methods often necessitate customization to specific optical systems or image sensors. HDR techniques relying on hardware modification are typically expensive and beyond the reach of average users.

Another class of approaches [25, 21, 36] is time-domain multi-frame fusion HDR, which merges a set of bracketed exposure LDR sRGB images to produce an HDR image. However, this process—capturing images from underexposed to overexposed configurations can result in blurring artifacts for moving objects. Sony has endeavored to address this by introducing the Digital Overlap (DOL) HDR sensor [6]. For instance, dual-exposure DOL sensors like Sony IMX327, IMX385, and OV OS05B produce long-exposure and short-exposure frames in line-interleaving patterns. This pattern significantly shortens the interval between these frames, thus minimizing relative motion. Presently, many methods use DOL sensors to capture a set of bracketed exposure raw images, which ISP processes, and subsequently fusion bracketed exposure LDR sRGB images to reconstruct an HDR image.

Recent trends in HDR imaging involve the application of deep neural networks [18, 26, 2] to learn the production of high-quality HDR images from a set of bracketed exposure LDR images. Kalantari et al. [16] propose a CNN-based HDR approach that employs optical flow to align LDR images before network inference. Wu et al. [36] approach HDR imaging as an image translation problem without explicit motion alignment. Yan et al. [37] introduce spatial attention to achieve LDR image alignment. Liu et al. [21] present an attention-guided deformable convolutional network for multi-frame HDR imaging. Prabhakar et al. [29] introduce an efficient method for generating HDR images using a bilateral guided up-sampler and explore zero-learning for HDR reconstruction. Niu et al. [27] propose a multi-frame HDR imaging method based on generative adversarial learning. Liu et al. [22] propose a Transformer-based [28] HDR imaging method. These deep learning-based approaches [37, 21, 22] consistently elevate state-of-the-art performance. However, these methods reconstruct HDR based on sRGB images at the end of the ISP pipeline and only train on one dataset. They overlook the large computational and storage resources required by the ISP pipeline to process bracketed exposure raw images. It also complicates the ISP system, making it challenging for resource-limited cameras to output high-quality

video/images.

## 2.2. Low-level Raw Image Processing

Learning-based processing of low-level raw images [19, 43] has received increasing attention. Google’s HDR+ [11] produces the raw HDR image by aligning and merging a burst of raw frames with the same low exposure. Zhang et al. [44] construct a real-world super-resolution dataset by designing an optical zoom system and propose a baseline network with a bilateral contextual loss. Qian et al. [30] solve the joint demosaicing, denoising, and super-resolution task with the raw input. Wang et al. [34] propose a lightweight and efficient network for raw image denoising. Sharif et al. [1] offer a new learning-based approach to tackle the challenge of joint demosaicing and denoising on image sensors. Wei et al. [35] investigate the low-light image denoising considering the sensor’s photoelectric properties. Yue et al. [42] achieve state-of-the-art raw image denoising by constructing a dynamic video dataset with noise-clean pairs.

Learning-based raw image processing has demonstrated outstanding potential for high-performance reconstruction from raw sensor data. However, acquiring paired data in the raw domain is difficult and expensive. Our work proposes a new large-scale, high-quality raw dataset and provides a pipeline to acquire raw LDR-HDR pairs based on the imaging system.

## 3. New raw LDR-HDR pair Formation Pipeline

We begin by analyzing the sensor response of the imaging system and presenting a novel data formation pipeline for raw LDR-HDR pairs based on the camera response model.

### 3.1. Analysis of CMOS Imaging System

The essence of a CMOS image sensor is photo-electric signal conversion. For a single pixel, the number of electrons  $Q$  released during the light-electric signal conversion can be ideally expressed as [12]:

$$Q = T \int_{\lambda} \int_x \int_y E(x, y, \lambda) S(x, y) q(\lambda) dx dy d\lambda, \quad (1)$$

where  $(x, y)$  represents spatial coordinates on the sensor plane,  $T$  is the integration time (exposure time),  $E(x, y, \lambda)$  signifies the incident spectral irradiance,  $S(x, y)$  characterizes the spatial response of the collection site, and  $q(\lambda)$  is defined as the ratio (electrons/Joule) of collected electrons per incident light energy for the sensor as a function of wavelength  $\lambda$ .

Given that  $(x, y)$  in Eq. 1 pertains to a single photosensory cell, we assume that each parameter remains con-

stant with respect to position. Consequently, the coordinates  $(x, y)$  can be omitted [14]:

$$Q = T\bar{S}A \int_{\lambda} E(\lambda)q(\lambda)d\lambda, \quad (2)$$

where  $\bar{S}$  denotes the expected value of  $S(x, y)$  within a single photosensory cell, and  $A$  denotes the effective photoreceptor area of the cell.

Subsequently, the camera's amplifier circuit amplifies the electrical signal, yielding the raw camera response value through analog-to-digital conversion [47]:

$$D = \frac{K_a Q + V_{\text{offset}}}{\eta} \times K_d, \quad (3)$$

where  $K_a$  represents the Analog Gain,  $K_d$  stands for the Digital Gain, and  $V_{\text{offset}}$  accounts for the bias voltage.  $\eta$  corresponds to the quantization step associated with the bit depth.

Combining Eq. 2 and Eq. 3, the ideal model for the optical-to-digital conversion is modeled as:

$$D = \frac{K_a T \bar{S} A \int_{\lambda} E(\lambda)q(\lambda)d\lambda + V_{\text{offset}}}{\eta} \times K_d, \quad (4)$$

where  $D$  signifies the pixel value in the raw image,  $V_{\text{offset}}/\eta$  accommodates artificially introduced bias voltage to prevent output signals below 0. The raw response value of the bias voltage (i.e., black level) can be directly read out. When the dark current is 0, or we subtract the raw response value of the bias voltage, the pixel value in the raw image can be expressed as:

$$D = \frac{K_a T \bar{S} A \int_{\lambda} E(\lambda)q(\lambda)d\lambda}{\eta} \times K_d, \quad (5)$$

We observe from Eq. 5 that under noise-free conditions, adjusting the gain factor ( $K_a, K_d$ ) can linearly adjust the camera's raw response value. This linear characteristic allows us to achieve an equivalent result as modifying the exposure time ( $T$ ) by simulating the Digital Gain, thereby obtaining a bracketed exposure raw image.

Nonetheless, due to noise in real-world imaging, changing the Digital Gain will also linearly amplify the noise. Therefore, to mitigate noise influence, we avoid this problem as much as possible during data acquisition (in Sec. 3.2.1). Also, we avoid using multiplicative gain to construct long-exposure images that amplify the noise difference between long- and short-exposure images and instead use truncation to similar long-exposure images. In addition, we synthesize the long-short exposure images by measuring the accurate HDR sensor noise model to eliminate the long-short exposure image noise difference. Based on this rationale, we propose an innovative and efficient pipeline for generating LDR-HDR data pairs.

### 3.2. Formation of Raw LDR-HDR Image Pair

Relative to sRGB images, HDR reconstruction from raw images offers several distinct advantages: it retains a more significant amount of original information and has higher bit depths, which is more beneficial for improving the dynamic range of the image; the Image Signal Processing (ISP) pipeline is more straightforward and less computational demands. These characteristics render raw HDR reconstruction a highly promising approach for deployment in edge devices. Considering these considerations, we create a raw HDR dataset featuring a collection of LDR-HDR data pairs, aptly named RealRaw-HDR.

#### 3.2.1 Data Acquisition

Based on the analysis in Sec. 3.1, we observe that changing the Digital Gain yields a comparable luminance to adjusting the exposure time when the noise level remains sufficiently low. Consequently, we can capture two raw images with identical exposure settings and subsequently manually simulate the Digital Gain to generate two raw images with differing exposures. It's crucial to emphasize that these two raw images with the same exposure require low noise and no overexposure. In order to capture near-noise-free raw images, we utilize high-end cameras, special photography techniques, and post-processing acquisitions.

Specifically, we use a top-of-the-line FUJI-FILM GFX50S II camera with a wide-aperture lens to capture high-quality raw images. The camera has a 51 megapixel medium format image sensor with a pixel size of  $5.3\mu\text{m}$  (The iPhone 14 Pro Max primary camera single pixel size is only  $1.22\mu\text{m}$ ). We also set the camera's ISO to 800 or below and turned on the noise reduction feature to enhance image quality. Subsequently, we subject the raw image to post-processing using the BM3D algorithm, attaining nearly noise-free raw images.

Meanwhile, to simulate the relative motion between long and short exposure images within a real-world scene, we use a human subject to simulate motion between LDR images and trigger the shutter twice in a rapid time interval. To eliminate the risk of unintended camera shake, we securely mount the camera on a tripod and use a remote smartphone to control the shutter release. Following image capture, the raw images undergo black level correction and normalization before being subjected to BM3D processing [23] to effectively reduce noise, thereby yielding raw images nearly devoid of noise.

#### 3.2.2 Data Processing

Fig. 2 shows the proposed data formation pipeline. Here's an in-depth breakdown of the data formation pipeline:

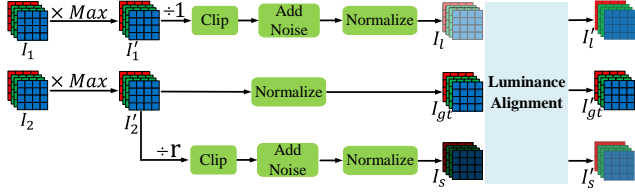


Figure 2. The raw LDR-HDR pair formation pipeline. Two clean high-bit raw images,  $I_1$  and  $I_2$ , have been processed through black-level correction, normalization, and BM3D denoising.

**Selection of exposure time ratio and initial adjustment.** Commencing the pipeline, we pack two clean Bayer raw images. We randomly select an exposure time ratio  $r$  from  $\{4, 8, 16\}$  at this stage.<sup>1</sup> The two normalized raw images, denoted as  $I_1$  and  $I_2$ , multiply by the maximum pixel value (Max:  $2^{12} \times r$ ). This operation yields  $I_1'$  and  $I_2'$  correspondingly.

**Long-exposure image simulation ( $I_l$ ).** Moving forward, we divide  $I_1'$  by 1 and then clip the pixel values to a range of 0 to 4095 (12 bit). This operation is equivalent to adjusting the Digital Gain ( $K_d$ ), achieving an outcome comparable to altering the exposure time. Subsequently, we synthesize the noisy image by long exposure image noise model measured by Sony IMX327 HDR sensor and normalize it. This process simulates a long-exposure noisy image ( $I_l$ ) reaching saturation signal level (full well capacity) and the inherent noise generated by the image sensor, which preserves dark detail while losing details in brighter areas.

**Short-exposure image simulation ( $I_s$ ).** Simultaneously, we divide  $I_2'$  by  $r$  and clip the pixel values to a range of 0 to 4095. (Equivalent to adjusting the Digital Gain). Similar to the previous step, synthesize the short-exposure noisy image by the short-exposure image noise model measured by the Sony IMX327 HDR sensor, and normalization follows suit. This procedure simulates a practical short-exposure image ( $I_s$ ). This image retains detail in highlighted portions but loses darker information due to noise interference.

**Ground truth image ( $I_{gt}$ ).** Additionally, we normalize  $I_2'$  to obtain the ground truth image  $I_{gt}$ . The  $I_{gt}$  contains more information on bright regions than  $I_l$ ;  $I_{gt}$  has a higher signal-to-noise ratio in dark regions compared to  $I_s$ . As a result, our data formation pipeline efficiently generates an extensive array of LDR-HDR data pairs.

**Luminance alignment.** Finally, after the luminance alignment [16], we obtain the noisy raw LDR images  $I_l'$  and  $I_s'$ , and the corresponding clean raw HDR image  $I_{gt}'$ .

The data formation pipeline facilitates the generation of rich LDR-HDR pairs, which is integral to our research and exploration.

<sup>1</sup>It's important to note that exposure ratios may not necessarily be multiples of 2.

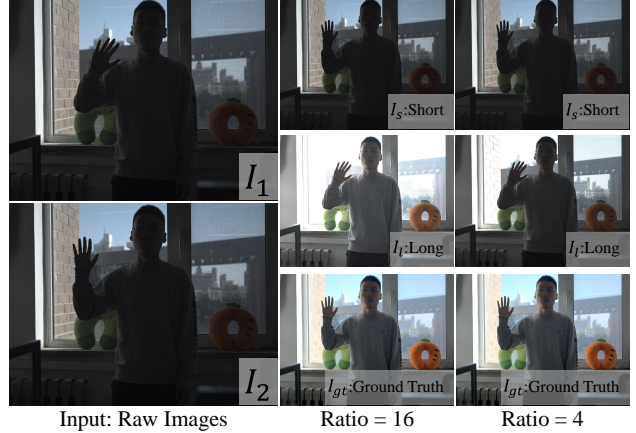


Figure 3. Real samples collected by the proposed raw LDR-HDR pair formation pipeline. For display purposes, we do not apply luminance alignment processing.

### 3.2.3 RealRaw-HDR Dataset

Our dataset is meticulously crafted for dual-exposure HDR sensors, supporting mainstream sensors, including Sony IMX327, IMX385, IMX585, and OV OS05B. To the best of our knowledge, there is an absence of a raw HDR dataset explicitly tailored for these HDR sensors. Furthermore, it is challenging to construct large-scale, high-quality raw HDR datasets from multi-exposed frames. Traditional methods of collecting HDR datasets often lead to misalignment issues, yielding fused HDR images of subpar quality; previous data collection methods necessitate subjects to remain static while capturing multiple exposures, a time-consuming and labor-intensive process. In contrast, our proposed raw LDR-HDR pair formation pipeline is efficient and user-friendly, enabling the effortless creation of a multitude of high-quality data pairs.

Through this pipeline, we gather 240 pairs of  $8192 \times 6192$  high-resolution raw LDR-HDR image pairs. Fig. 3 shows an example of two generated LDR-HDR pairs with different exposure ratios. Additionally, by attaching an ISP pipeline to the end of our pipeline, we can create an sRGB-based HDR training dataset. In Tab. 1, we compare the statistics of our dataset with those of other existing HDR datasets.<sup>2</sup>

## 4. The Proposed RepUNet Network

HDR reconstruction plays a vital role in various applications, such as mobile photography, high-definition displays, and virtual reality, where lightweight and efficient algorithms are highly demanded due to resource limitations. Previous learning-based HDR methods [22, 21, 16]

<sup>2</sup>If not specified, all raw images in this paper have been processed by a fixed ISP to obtain sRGB versions for visualization purposes.

Table 1. Comparison with existing HDR datasets.  $\times 3$  indicates that the same set of images can be expanded with three exposure ratios. Theoretically, Our dataset can be expanded  $N$  times by the raw LDR-HDR pair formation pipeline,  $N$  denotes the number of covered exposure ratios.

Data	Quantity	Size	Format	Exposure Ratio
Kalantri [16]	74	1490 $\times$ 989	sRGB	{4, 8, 16}
Chen [5]	144	4096 $\times$ 2168	raw, sRGB	{4, 8, 16}
Ours	240 $\times$ 3	8192 $\times$ 6192	raw, sRGB	{4, 8, 16}

often rely on large and complex models, making them impractical for real-world scenarios. Therefore, we propose a UNet-like lightweight base model, DualUNet, to address this challenge and employ reparameterization techniques to improve its representation capability while balancing storage and computation cost and reconstruction accuracy. We first present the DualUNet and then develop our RepUNet by reparameterization, followed by the design of the loss function.

#### 4.1. Base Model of DualUNet

To ensure high inference speed and cross-device deployment on commodity mobile devices, we carefully consider the limited computation and memory resources on mobile devices and deliberately choose a UNet-like network as the base model, namely DualUNet. The overall architecture of the DualUNet is shown in Fig. 4(a). We do not use the computationally demanding explicit alignment in our HDR network for lightweight design. We introduce an alignment-free and motion-aware short-exposure-first selection loss (in Sec. 4.3) that enables training with unaligned pairs to compensate for the absence of alignment modules.

We first use the pixel unshuffle operation [10] to transfer the input raw images  $I'_s$  and  $I'_l$  from  $C \times H \times W$  to  $4C \times \frac{1}{2}H \times \frac{1}{2}W$  to extract large-scale contextual information while maintaining low computational complexity. Notably, short-exposure images have less motion blur distortion but severe noise in dark areas. Conversely, long-exposure images generally contain more information with a higher signal-to-noise ratio but may suffer from significant motion blur and overexposure.

To better leverage the complementary information from the two types of images, we introduce two distinct sub-encoders: Encoder-S and Encoder-L. Encoder-S extracts features from the short-exposure image, serving as foundational reference features. In parallel, Encoder-L extracts features from the long-exposure image, offering supplementary features. We fuse the multi-scale features using addition or concatenation operations at each feature level to facilitate complementary features to learn motion information from the reference features.

Each Encoder-S consists of a pixel unshuffle  $\downarrow 2$  downsampling operation, a  $3 \times 3$  convolution layer, and a ReLU activation ([Down-Conv-ReLU]). At the same time, the

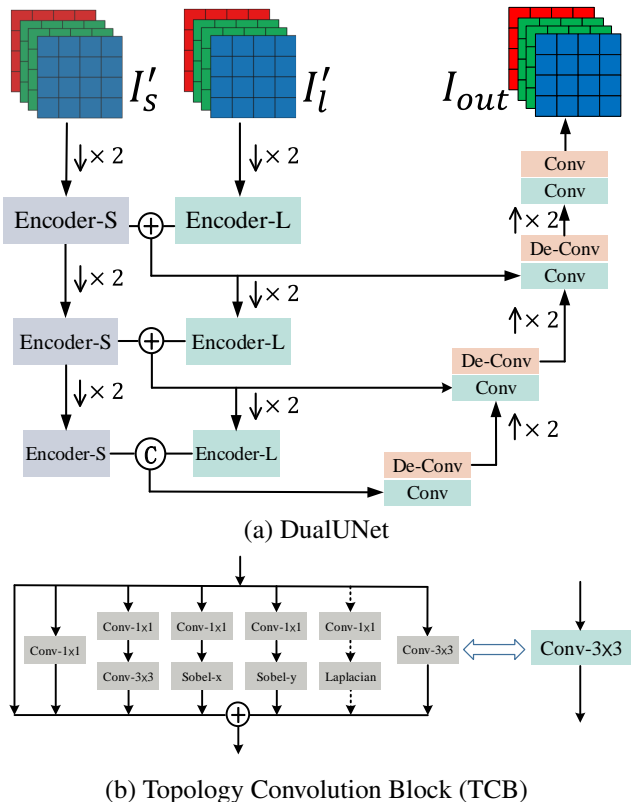


Figure 4. Illustration of (a) DualUNet and (b) Topology Convolution Block (TCB). In the training phase, the TCB module replaces the normal convolution, which is merged back into a normal  $3 \times 3$  convolution layer in the inference phase.

Encoder-L has the structure of [Down-Conv-ReLU-ConvReLU]. The pixel unshuffle operation can avoid information loss introduced by conventional downsampling/pooling operations. Finally, the fused features are fed into the decoder to generate the final HDR output.

#### 4.2. RepUNet Network

The representation capability of the plain DualUNet for HDR imaging is significantly limited, as shown in Tab. 6, leading to unsatisfactory performance. To address this concern, we introduce a flexible re-parameterizable module called the Topological Convolution Block (TCB) and replace the normal convolution in DualUNet with the TCB module during the training phase. Notably, the last layer of DualUNet is still a normal convolution.

Although the reparameterization has achieved promising results on other tasks [9, 4, 7, 46], its application in reparameterization blocks for low-level visual tasks remains scarce. We integrate previous reparameterization blocks and flexibly design reparameterization blocks with six operator combinations to enhance the feature representation of the model for HDR and denoising tasks. The TCB consists of sev-

eral fundamental units: (1) a standard  $3 \times 3$  convolution for a solid foundation; (2) extending and squeezing convolution to enhance feature expressiveness, (3) Sobel and Laplacian operators for extracting first and second-order spatial derivatives to identify edges; (4) a jump connection to avoid gradient vanishing or exploding, and (5) a  $1 \times 1$  convolution to encourage information exchange between channels. It's paramount to underscore that we exclusively employ the TCB with the Laplacian operator within the decoder. This selective approach is grounded in Laplacian operator effectiveness for noise-free images, underpinning its application to enhance feature representation in contexts devoid of noise.

To achieve an efficient HDR network that meets the stipulated design prerequisites of low computational complexity and streamlined hardware device deployment, we simplify the TCB reparameterization into a single  $3 \times 3$  convolution after training. Following previous works [8, 7, 46], we leverage the additivity and homogeneity of convolutions, and we merge the  $1 \times 1$  extending and  $3 \times 3$  squeezing convolution into a normal  $3 \times 3$  convolution. Additionally, we combine the Sobel and Laplacian operators into a special  $3 \times 3$  convolution with a fixed convolution kernel. The  $1 \times 1$  convolution is achieved by padding the convolution kernel with zeros. As a result, TCB can be transformed into a single  $3 \times 3$  convolution for efficient implementation during the inference stage. By utilizing TCB, we achieve superior HDR results with improved efficiency.

### 4.3. Loss Functions

**Alignment-free and motion-aware short-exposure-first selection loss.** In fused-based HDR imaging, eliminating ghosting caused by motion inconsistencies between short and long frames is one of the most challenging issues. Previous work [16, 37] commonly employs optical flow, attention mechanisms, and other methods to establish pixel correspondences between long and short frames. The objective is to suppress ghosting by designing more elaborate fusion strategies. Yet, these motion estimation and alignment methods are often the most computationally intensive components and cannot be accommodated by the current level of hardware design. To ensure fast inference and easy hardware deployment, we abandon explicit motion alignment schemes and instead explore a more efficient alternative. Consequently, we introduce a plug-and-play alignment-free and motion-aware short-exposure-first selection loss to mitigate the ghost artifacts.

Unlike other tasks involving image alignment, such as video motion estimation and stereo matching, long and short-exposure image fusion in HDR reconstruction does not necessarily require pixel-level correspondence in real-world scenes. The reason is that it is challenging to recover sharp object edges due to motion blur. In contrast, short-

exposure images exhibit less motion blur distortion. Therefore, ghost artifacts can be suppressed by simply detecting motion regions in long-frame images through some mechanism, discarding these pixels during the fusion process, and relying solely on the corresponding regions in short-exposure images as the exclusive information source for fusion. Based on the same consideration, overexposed regions in the long-exposure image should likewise be discarded from the fusion process. Therefore, in practical engineering applications, short exposures are often used as reference images.

Based on the above analysis, we devise the following strategies for double-exposure HDR fusion: in scenarios involving motion or overexposure within the fused region, we prefer to select the short-exposure image that contains more information; when the signal-to-noise ratio of the short frame is too low, we prefer to select the long-exposure image that contains more information. It is worth noting that our strategy is inclined to address motion artifacts with a higher priority than low signal-to-noise ratios. Consequently, when both ghost artifacts and low signal-to-noise ratios are concurrently evident, the short-exposure image is chosen to prioritize the motion artifacts.

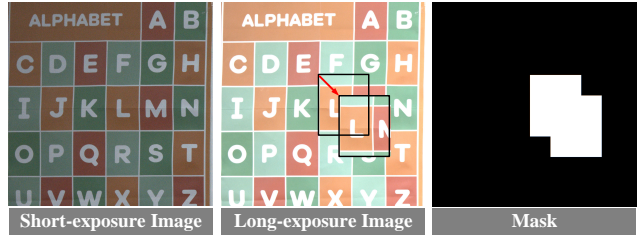


Figure 5. An illustrative sample of data construction for the proposed pseudo location-based motion alignment loss.

Note that after the luminance alignment, the long and short frames already have similar luminance levels, and the regions with remarkable luminance differences are mainly caused by motion and overexposure. Therefore, we expect the network to perceive the motion and overexposed regions by focusing on the luminance gap between the long and short exposures, thereby realizing the short-frame prioritization strategy mentioned above. For this purpose, we design an alignment-free and motion-aware short-exposure-first selection loss function.

$$L_{AMSS} = 1 - MSSSIM(\tilde{I}^{out} \odot M, I^{gt} \odot M), \quad (6)$$

where  $\odot$  denotes the point-wise multiplication, and  $M$  is a binary mask with “1” for motion regions in long frames, and “0” otherwise. Given a mask  $M$  indicating motion and overexposed regions, the above loss formula implements a strategy that encourages short-frame prioritization.

To avoid explicit motion alignment, we adopt the synthetic motion to construct the mask  $M$  in the training

quadruplets  $\{I'_l, I'_s, M, I'_{gt}\}$ . Specifically, as shown in Fig. 5, for each patch of an image, we randomly select a rectangle (40 to 60-pixel range) of random length and width from the long-exposure image and then move and overlap it to a random location in the range of -30 to 30 relative to the patch. The patch regions before and after the movement are labeled as 1s in the mask  $M$ . By introducing the mask  $M$  to guide the network to focus on moving and overexposed regions, the model effectively prioritizes the short-exposure information over the long-exposed counterpart within these regions. The masks are used only in training, and the inference stage inputs only short and long exposure frames.

**Reconstruction loss.** For saturated areas, the L2 loss punishes any deviation of pixel values from the ground truth. This allows the model to select short-exposure information in over-exposed areas. To achieve the best HDR reconstruction results, we employ the MS-SSIM loss guide model, which learns short-exposure image information for global motion. By combining these loss functions, our model effectively produces superior results for both areas

with motion and saturated regions.

$$L_{\text{pix}} = \|\tilde{I}^{\text{out}} - I^{\text{gt}}\|_2, \quad (7)$$

$$L_{\text{ssim}} = 1 - \text{MSSSIM}(\tilde{I}^{\text{out}}, I^{\text{gt}}). \quad (8)$$

**Bayer loss.** We propose a color correction loss, named Bayer loss, to minimize color cast and artifacts. We average the two G channels of the output (RGGB pattern) and ground truth (RGGB pattern) respectively, and then concatenate the averaged G channel with the R and B channels to perform a naive transformation to the RGB color space, producing two RGB images:  $\tilde{I}_{\text{rgb}}^{\text{out}}$  and  $I_{\text{rgb}}^{\text{gt}}$ . Then, we impose the colorfulness loss between the processed output and ground truth by the cosine embedding loss.

$$L_{\text{b}} = \text{Cosine}(\tilde{I}_{\text{rgb}}^{\text{out}}, I_{\text{rgb}}^{\text{gt}}), \quad (9)$$

where Cosine denotes cosine embedding loss [32]. The overall loss function is

$$L = \alpha \cdot L_{\text{AMSS}} + \beta \cdot L_{\text{b}} + \gamma \cdot L_{\text{pix}} + \eta \cdot L_{\text{ssim}}. \quad (10)$$

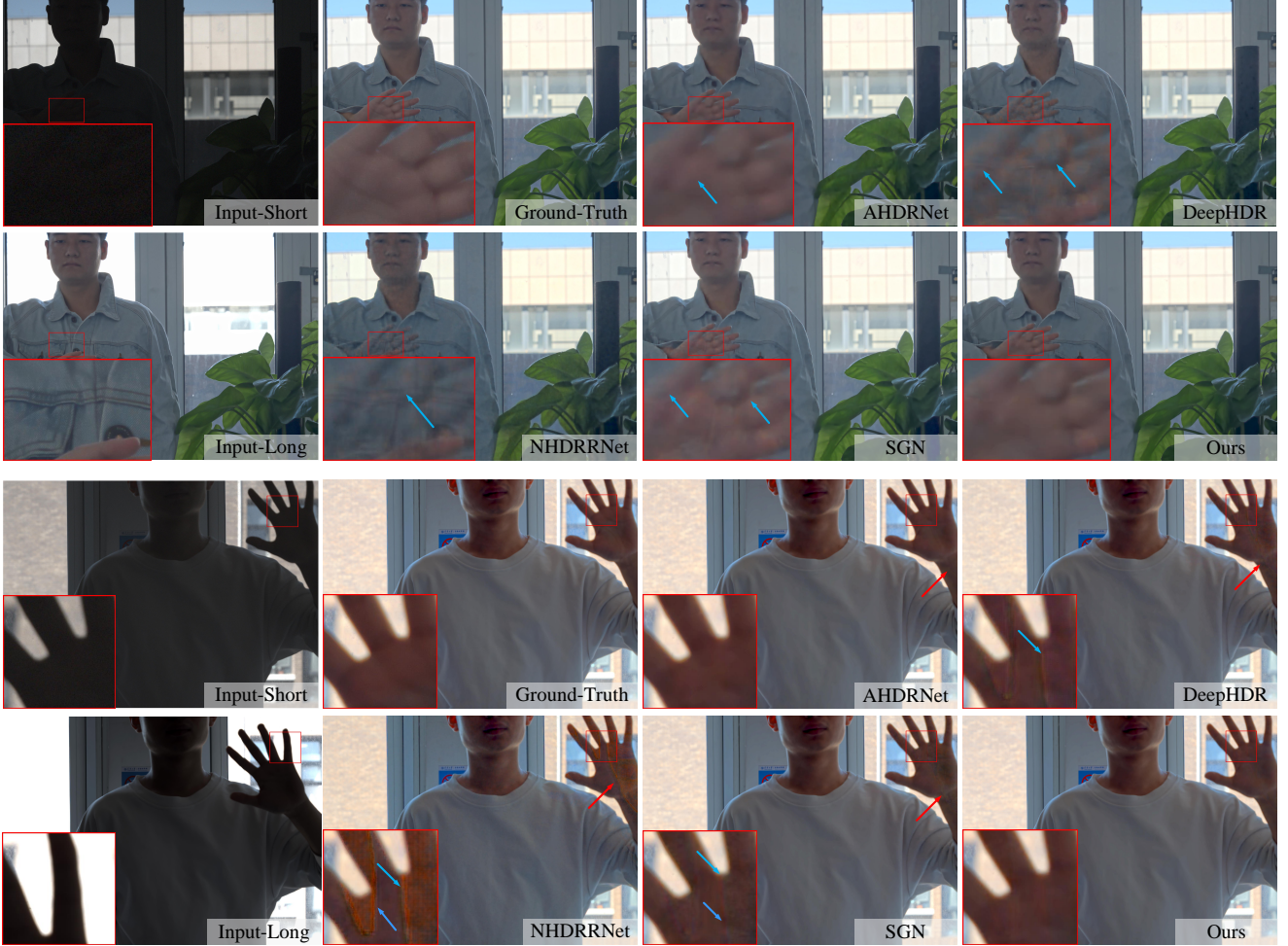


Figure 6. Visual comparison of state-of-the-art HDR reconstruction methods on our synthetic test dataset.

Table 2. Performance comparison of different HDR models on our synthetic dataset. Params and FLOPs represent the total number of network parameters and floating-point operations. The FLOPs and Run Times results are measured on an RTX 3090 device with a resolution of  $4096 \times 2952$  raw images. Metrics with  $\uparrow$  and  $\downarrow$  denote higher better and lower better, respectively. The best and second-best performances are in bold and underlined, respectively. “-” indicates the result is not available.

Methods	FLOPs	Params	Run Time	All-Exposure		Ratio=4		Ratio=8		Ratio=16	
				PSNR $\uparrow$	$\Delta E \downarrow$						
DeepHDR[16]	2409.32G	15.26M	4.3 ms	43.3680	1.3767	43.5551	1.3844	43.7312	1.3679	42.8178	1.3779
NHDRRNet[40]	826.17G	40.26M	7.9 ms	33.0206	2.7308	33.0127	2.7277	33.0392	2.7203	33.0101	2.7443
UNet-SID[3]	<u>640.89G</u>	7.76M	<u>3.1 ms</u>	44.3892	1.3434	44.3314	1.3535	44.4551	1.3312	44.3811	1.3456
SGN[10]	712.66G	4.78M	3.3 ms	44.6094	1.3235	44.5074	1.3398	44.7078	1.3067	44.6131	1.3240
HDR-Transformer[22]	3698.28G	1.23M	-	44.3895	1.3681	44.3311	1.3811	44.4140	1.3619	44.4235	1.3613
AHDRNet[37]	2848.29G	0.93M	23.6 ms	<u>44.7985</u>	<u>1.2939</u>	<b>44.8548</b>	<b>1.2957</b>	<u>44.8343</u>	<u>1.2892</u>	<u>44.7064</u>	<u>1.2968</u>
Ours	<b>127.55G</b>	<b>0.82M</b>	<b>2.9 ms</b>	<b>44.8081</b>	<b>1.2886</b>	44.7575	1.3000	<b>44.8482</b>	<b>1.2812</b>	<b>44.8187</b>	<b>1.2842</b>



Figure 7. Visual comparisons with the state-of-the-art methods on HDR sensor raw dataset.

where  $\alpha$ ,  $\beta$ ,  $\gamma$ , and  $\eta$  are the corresponding weight coefficients.

## 5. Experiments

### 5.1. Experimental Setup

**Datasets and Metrics.** We utilize the proposed RealRaw-HDR dataset for training. For testing, we first evaluate our method on the dataset, which is synthesized using the data formation pipeline. This dataset was not utilized during training. This test set contains 30 sets of test samples containing different exposure ratios (i.e., 4, 8, and 16) with a resolution of  $4096 \times 2176$ . To validate the generalization ability of our method on real data, we utilize a FUJI-FILM GFX50S II camera to capture seven sets of real-

world bracketed exposure raw images and the corresponding static images for generating the ground truth. Furthermore, to validate the generalization ability of our method on HDR sensors, we utilize Chen’s test dataset [5] for cross-validation, which has short-long raw images captured by a Sony IMX267 image sensor.

We perform a quantitative evaluation using the PSNR, SSIM, and CIE L\*a\*b\* space<sup>3</sup> [45, 13, 20] (also known as  $\Delta E$ ).  $\Delta E$  can effectively assess chromaticity, contrast, and color accuracy variations within HDR images rather than exclusively concentrating on luminance differences (HDR-

<sup>3</sup>CIE L\*a\*b\* is a color space specified by the International Commission on Illumination. It describes all the colors visible to the human eye and was created to serve as a device-independent model to be used as a reference.

Table 3. Performance comparison of different HDR models on the actual HDR sensor raw dataset [5]. The best and second-best performances are in bold and underlined, respectively.

Methods	All-Exposure			Ratio=4			Ratio=8			Ratio=16		
	PSNR↑	SSIM↑	ΔE ↓									
DeepHDR[16]	39.4902	0.9731	2.0670	39.2987	0.9716	2.1201	40.3268	0.9779	1.9159	38.8450	0.9697	2.1648
NHDRRNet[40]	30.4292	0.9640	5.2132	30.5489	0.9615	5.0771	30.6833	0.9704	5.1679	30.0553	0.9601	5.3945
UNet-SID[3]	39.6099	<u>0.9735</u>	2.1527	39.4473	<u>0.9723</u>	2.1860	40.4429	0.9772	1.9640	38.9394	0.9712	2.3081
SGN[10]	39.3674	0.9727	2.3317	39.3531	0.9718	2.3357	40.0126	0.9761	2.1956	38.7366	0.9704	2.4639
HDR-Transformer[22]	39.9483	0.9726	2.1241	39.7823	0.9715	2.1859	40.5929	0.9750	2.0068	39.4698	<u>0.9713</u>	<u>2.1793</u>
AHDRNet[37]	40.4131	0.9695	<u>2.0123</u>	<b>40.4692</b>	0.9677	<u>1.9829</u>	<u>41.0748</u>	0.9717	<u>1.8519</u>	39.6953	0.9692	2.2025
Ours	<b>40.5238</b>	<b>0.9747</b>	<b>1.9568</b>	40.4061	<b>0.9733</b>	<b>1.9743</b>	<b>41.4010</b>	<b>0.9788</b>	<b>1.7974</b>	<b>39.7642</b>	<b>0.9721</b>	<b>2.0988</b>

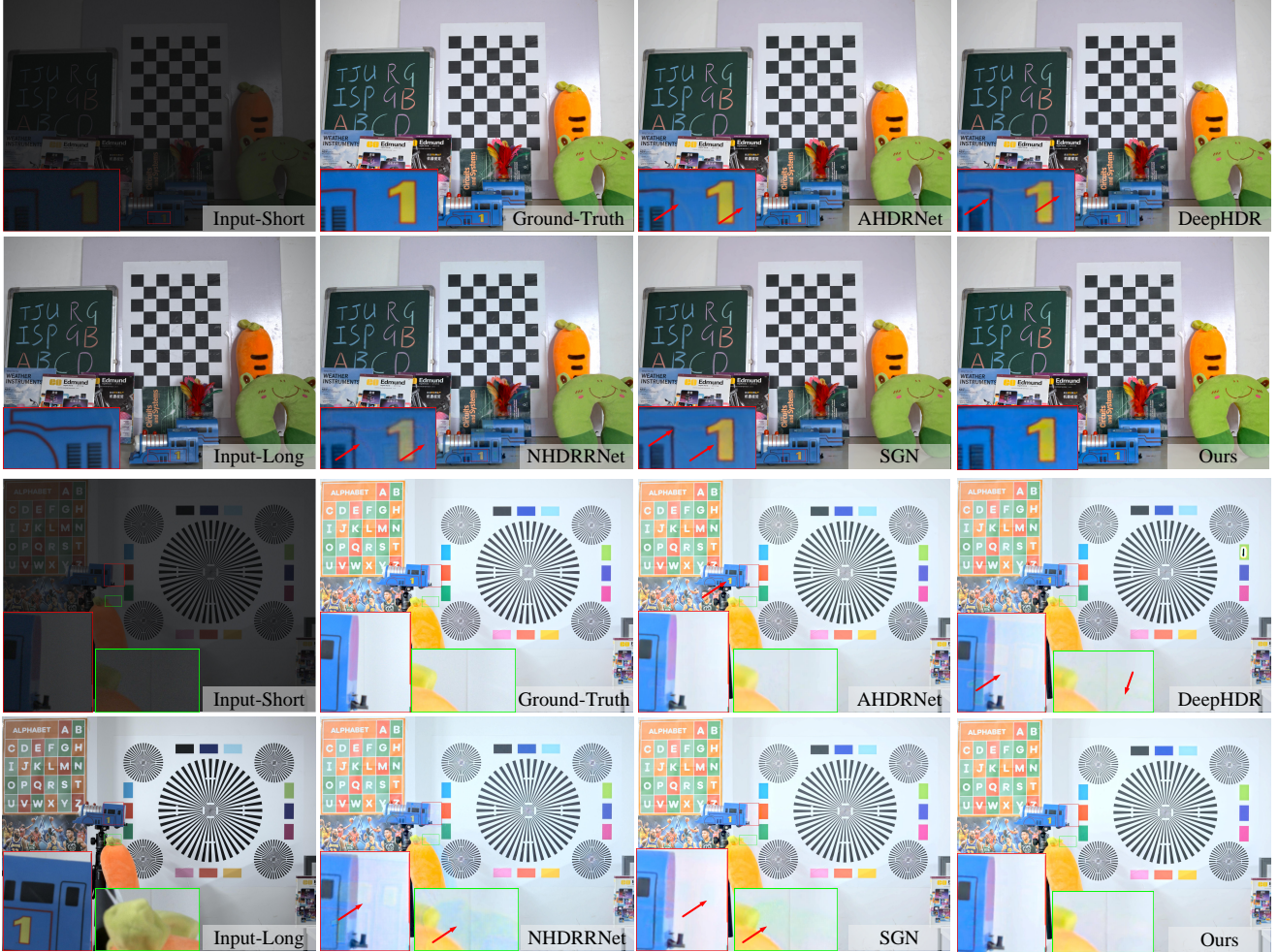


Figure 8. Visual comparison of state-of-the-art HDR reconstruction methods on RealRaw-HDR dataset with realistic exposure ratios.

VDP-2). It offers a comprehensive quality evaluation by measuring the disparity between two HDR images within the CIE Lab color space.

$$\Delta E = \|\tilde{I}_{lab}^{out} - I_{lab}^{gt}\|_2, \quad (11)$$

where  $\tilde{I}_{lab}^{out}$  and  $I_{lab}^{gt}$  are the CIE Lab version of the predicted HDR image and ground truth, respectively.

**Implementation Details.** We train our model using the Adam optimizer [17] with weight decay  $1 \times 10^4$ , learning

rate  $10^{-4}$ , and  $\beta_1$  and  $\beta_2$  values set to 0.9 and 0.999, respectively. The input patch size for the network is  $256 \times 256$ , and the batch size is 32. Our model is implemented in PyTorch and trained with an NVIDIA RTX 3090 GPU.

## 5.2. Comparison with the State-of-the-art Methods

We choose several representative low-level vision methods for comparisons, including four HDR methods based on sRGB images (AHDRNet [37], DeepHDR [16], NHDR-

Table 4. Quantitative comparisons of different loss functions. AMSS-Loss represents the alignment-free and motion-aware short-exposure-first selection loss.

ID	Method	Bayer-Loss	AMSS-Loss	All-Exposure		Ratio=4		Ratio=8		Ratio=16	
				PSNR↑	ΔE↓	PSNR↑	ΔE↓	PSNR↑	ΔE↓	PSNR↑	ΔE↓
1	RepUNet	✗	✗	39.6403	2.1479	39.5214	2.1577	40.5216	<u>1.9603</u>	38.8780	2.3256
2	RepUNet	✓	✗	40.0251	<u>2.1162</u>	39.9900	<u>2.1143</u>	<u>40.8125</u>	1.9700	39.2729	<u>2.2642</u>
3	RepUNet	✓	✓	<b>40.5238</b>	<b>1.9568</b>	<b>40.4061</b>	<b>1.9743</b>	<b>41.4010</b>	<b>1.7974</b>	<b>39.7642</b>	<b>2.0988</b>

RNet [40], HDR-Transformer[22]), as well as two methods for denoising raw images (SGN [10] and UNet-SID [3]). For fair comparisons, we re-train all the methods using the RealRaw-HDR dataset. Additionally, for AHDRNet, DeepHDR, HDR-Transformer, and NHDRRNet, we modify the network inputs to accommodate dual-exposure raw images. Similarly, for SGN and UNet-SID, we concatenate the long- and short-exposure images as inputs.

**Evaluation on synthetic dataset.** We first evaluated our method on a synthetic dataset generated using the raw HDR data formation pipeline. The quantitative comparison results are shown in Tab. 2. The results clearly show that our method outperforms previous methods in almost all metrics on the synthetic dataset. Notably, our lightweight-efficient RepUNet model has fewer parameters (0.82M) and remarkably low GFLOPs (127G FLOPs). This efficiency allows us to process two 4K Bayer raw images at only 2.9ms using an NVIDIA RTX 3090 GPU. In contrast, other models with comparable performance necessitate significantly longer processing times. RepUNet achieves comparable performance with AHDRNet with only 4.5% of its computational complexity (127G vs. 2848G). Fig 6 visualizes that our method can effectively eliminate noise and ghosting artifacts in the reconstructed HDR. In comparison, DeepHDR [16], NHDRRNet [40], and SGN [10] exhibit numerous artifacts in the palm motion region. However, our proposed RepUNet can reconstruct HDR images without ghosting (see rows 2 and 4).

**Evaluation on HDR sensor raw dataset.** To validate the generalization ability of our method on the real-world HDR sensor, we utilize Chen’s test dataset [5] for cross-validation, which has raw images captured by a Sony IMX267 image sensor. Compared with previous methods, our method achieves state-of-the-art performance in terms of both visual quality and quantitative metrics. The visual results from tests on the HDR sensor raw dataset (as shown in Fig. 7) indicate that DeepHDR, NHDRRNet, and SGN show noticeable ghosting, with NHDRRNet also suffering from severe color casts. Furthermore, results in Tab. 3 reveal that compared to AHDRNet [37], our method yields an improvement of more than 0.35 dB and 0.05 gain in PSNR and  $\Delta E$ , respectively, for scenes with an exposure ratio of 8. On average, our method attains gains exceeding 0.1 dB and 0.15 in these metrics.

**Evaluation on FUJI raw dataset.** We then evaluate

our method on the FUJI raw datasets, which are real-world bracketed exposure raw images captured by the FUJI-FILM GFX50S II camera. Fig. 8 compares results from two high dynamic range scenes, where our method achieves significantly better visualization. Our method can recover both fine details in overexposed regions and rich colors in underexposed areas without introducing artifacts (see rows 1 and 2). Compared to AHDRNet, our method can effectively remove noise and preserve the structure of dark regions. Notably, the alignment module in DeepHDR, AHDRNet, HDR-Transformer, and NHDRRNet requires many line buffers, making it challenging to deploy on resource-limited edge devices. Notably, HDR-Transformer fails to perform inference even on RTX 3090 devices. In contrast, our method can alleviate ghost artifacts without relying on any alignment module and addresses color cast issues in raw images, as evident in the visual results of Fig. 6, Fig. 7, and Fig. 8.

Table 5. Performance comparison of different HDR models on RealRaw-HDR dataset with realistic exposure ratios. The FLOPs are measured on the raw image of  $7808 \times 5824$  resolution. The best and second-best performances are in bold and underlined, respectively.

Methods	FLOPs	PSNR↑	SSIM↑	ΔE↓
DeepHDR[16]	8987.98G	40.3610	0.9740	1.5235
NHDRRNet[40]	3081.94G	<u>33.3725</u>	0.9694	2.8789
UNet-SID[3]	<u>2390.83G</u>	41.9495	0.9751	1.4881
SGN[10]	2658.57G	41.8942	0.9750	1.4874
HDR-Transformer[22]	13946.42G	41.9963	0.9753	1.4897
AHDRNet[37]	10625.58G	<b>42.6409</b>	<b>0.9763</b>	<b>1.4004</b>
Ours	<b>475.83G</b>	42.5364	0.9760	1.4101

Despite the fact that all models are trained on the RealRaw-HDR dataset, which is synthesized using the data formation pipeline, they consistently excel on both the synthetic test set and the real-world dataset. Particularly noteworthy is the remarkable performance achieved on the test set comprised of raw images captured by the HDR sensor [5]. These results serve as solid evidence of the generalizability of our proposed RealRaw-HDR dataset and the HDR data formation pipeline. It underscores the robustness inherent in our approach and its capacity to tackle real-world challenges. This not only validates the efficacy of our methodology but also highlights its considerable potential for diverse real-world applications.

Table 6. Reparameterization ablation results. The FLOPs and Run Times are measured on the raw image of 4K resolution.

Method	FLOPs	Params	Run Times	All-Exposure		Ratio=4		Ratio=8		Ratio=16	
				PSNR↑	ΔE ↓						
DualUNet	93.26G	0.82M	3.0 ms	39.7941	2.1202	39.8026	2.1036	40.5092	1.9790	39.0705	2.2780
DualUNet <sub> tcb</sub>	250.79G	2.16M	70.1 ms	40.5220	1.9573	40.4051	1.9746	41.3990	1.7978	39.7620	2.0995
RepUNet	93.26G	0.82M	2.9 ms	<b>40.5238</b>	<b>1.9568</b>	<b>40.4061</b>	<b>1.9743</b>	<b>41.4010</b>	<b>1.7974</b>	<b>39.7642</b>	<b>2.0988</b>

### 5.3. Ablation Study

This section investigates the raw LDR-HDR pair formation pipeline and the importance of different components in the whole RepUNet. We ablate the baseline model step by step and compare the performance differences.

**Generalization of our LDR-HDR pair formation pipeline.** Our raw LDR-HDR pair formation pipeline is proposed to generate paired raw LDR-HDR data but can also be adapted to generate paired sRGB HDR data. To demonstrate such generalization, we transform the collected RealRaw-HDR dataset with a fixed ISP pipeline into the sRGB color space, named the Raw2RGB-HDR dataset. For comparison, we train the sRGB HDR method AHDRNet [37] on our Raw2RGB-HDR dataset (240 pairs) and Kalantari’s dataset [16] (taking the first two exposures as input, 74 pairs of images), respectively. The test dataset is from Kalantari’s dataset. Results in Tab. 7 show that AHDRNet trained on our Raw2RGB-HDR dataset outperforms the one trained on Kalantari’s dataset by 2.86 dB in PSNR. The performance gains benefit from an efficient and user-friendly data acquisition pipeline that generates more trainable data pairs. The results demonstrate that our data pipeline is also effective in generating paired LDR-HDR data in sRGB space.

Table 7. We train the sRGB HDR method AHDRNet on our Raw2RGB-HDR dataset (240 pairs) and Kalantari’s dataset, respectively. RealRGB-HDR is obtained by processing the RealRaw-HDR dataset.

Method	Dataset	PSNR	PSNR- $\mu$
AHDRNet	Kalantari	35.4581	38.1618
AHDRNet	Raw2RGB-HDR	<b>38.3183</b>	<b>39.8896</b>

**Loss Functions.** To test the effects of alignment-free and motion-aware short-exposure-first selection loss and Bayer loss, we set the  $L_2$  joint  $L_{ssim}$  loss as the baseline loss and step-by-step modify the loss function combination. Tab. 4 and 9 show that adding the AMSS loss and Bayer loss steadily improves visual quality and quantitative results. RepUNet with joint loss achieves the best results, outperforming the baseline by 0.5 dB in PSNR and by 0.16 in  $\Delta E$  on average. As Fig. 9 shows, alignment-free and motion-aware short-exposure-first selection loss (AMSS-Loss) effectively suppresses the ghosting artifacts (see columns 3 and 4). Meanwhile, our proposed Bayer loss can alleviate the color cast (see columns 2 and 3).

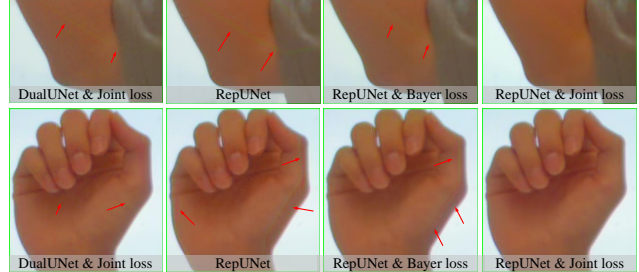


Figure 9. Visual results of RepUNet and its baseline variants. By combining these loss functions, our model can effectively produce top-notch results for both motion and saturated areas.

**Model reparameterization.** Tab. 6 presents the results for the DualUNet, DualUNet with TCB (DualUNet <sub>tcb</sub>; before reparameterization), and RepUNet. The RepUNet enjoys the same low complexity as the base model (DualUNet) and shares even slightly higher reconstruction performance than RepUNet <sub>tcb</sub>, which validates the effectiveness of our proposed TCB module. As can be seen, the enhanced models again obtain  $> 0.7$  dB consistent improvement on the PSNR index. This indicates that our TCB is a general drop-in replacement module for improving HDR performance without introducing additional inference costs.

## 6. Discussion and Future Work

Although our method can produce high-quality HDR images in real scenes, it has several limitations that may inspire future work.

Our data synthesis pipeline employs noise simulation to synthesize long and short-exposure images. However, we have found that if the noise distribution of the images we test is significantly different from the noise model we have measured, the results of the reconstruction are often unsatisfactory. Nevertheless, for practical engineering applications, it is important to accurately measure each type of image sensor noise model to achieve efficient raw denoising.

Furthermore, our work does not cover scenarios involving flicker. This is because the flicker problem generally arises in short-exposure images, and it is difficult to determine which region is better when flicker and motion occur simultaneously. Unfortunately, there is no clear-cut solution that can effectively address scenes where both flicker and motion are present. To overcome this challenge, it may be necessary to create a flicker model to generate a substan-

tial amount of training data.

## 7. Conclusion

We propose a novel data formation pipeline for raw LDR-HDR pairs based on HDR sensor imaging systems and construct a new high-quality raw dataset and raw LDR-HDR pairs dataset. This dataset can efficiently support many kinds of dual-exposure HDR sensor development, which provides vital data support for realizing the new generation of AI ISPs. Meanwhile, we develop a lightweight and efficient RepUNet network that uses structural reparameterization for HDR image reconstruction. Our evaluation has shown that this model can be easily deployed on mobile devices. We propose a plug-and-play alignment-free and motion-aware short-exposure-first selection loss and Bayer loss to address the issue of ghosting artifacts and color cast. Extensive experiments demonstrate that our approach achieves state-of-the-art performance in both visual quality and quantitative metrics.

## References

- [1] SM A Sharif, Rizwan Ali Naqvi, and Mithun Biswas. Beyond joint demosaicking and denoising: An image processing pipeline for a pixel-bin image sensor. In *Proceedings of the IEEE/CVF Conference on Computer Vision and Pattern Recognition*, pages 233–242, 2021.
- [2] Meng Chang, Huajun Feng, Zhihai Xu, and Qi Li. Low-light image restoration with short- and long-exposure raw pairs. *IEEE Transactions on Multimedia*, page 702–714, Jan 2022.
- [3] Chen Chen, Qifeng Chen, Jia Xu, and Vladlen Koltun. Learning to see in the dark. In *Proceedings of the IEEE conference on computer vision and pattern recognition*, pages 3291–3300, 2018.
- [4] Chengpeng Chen, Zichao Guo, Haien Zeng, Pengfei Xiong, and Jian Dong. Repghost: A hardware-efficient ghost module via re-parameterization. *arXiv preprint arXiv:2211.06088*, 2022.
- [5] Guanying Chen, Chaofeng Chen, Shi Guo, Zhetong Liang, Kwan-Yee K Wong, and Lei Zhang. Hdr video reconstruction: A coarse-to-fine network and a real-world benchmark dataset. In *Proceedings of the IEEE/CVF International Conference on Computer Vision*, pages 2502–2511, 2021.
- [6] L. Chermak and N. Aouf. Enhanced feature detection and matching under extreme illumination conditions with a hdr imaging sensor. In *IEEE International Conference on Cybernetic Intelligent Systems*, 2012.
- [7] Xiaohan Ding, Yuchen Guo, Guiguang Ding, and Jungong Han. Acnet: Strengthening the kernel skeletons for powerful cnn via asymmetric convolution blocks. In *Proceedings of the IEEE/CVF international conference on computer vision*, pages 1911–1920, 2019.
- [8] Xiaohan Ding, Xiangyu Zhang, Jungong Han, and Guiguang Ding. Diverse branch block: Building a convolution as an inception-like unit. In *Proceedings of the IEEE/CVF Conference on Computer Vision and Pattern Recognition*, pages 10886–10895, 2021.
- [9] Xiaohan Ding, Xiangyu Zhang, Ningning Ma, Jungong Han, Guiguang Ding, and Jian Sun. Repvgg: Making vgg-style convnets great again. In *Proceedings of the IEEE/CVF conference on computer vision and pattern recognition*, pages 13733–13742, 2021.
- [10] Shuhang Gu, Yawei Li, Luc Van Gool, and Radu Timofte. Self-guided network for fast image denoising. In *Proceedings of the IEEE/CVF International Conference on Computer Vision*, pages 2511–2520, 2019.
- [11] Samuel W. Hasinoff, Dillon Sharlet, Ryan Geiss, Andrew Adams, Jonathan T. Barron, Florian Kainz, Jiawen Chen, and Marc Levoy. Burst photography for high dynamic range and low-light imaging on mobile cameras. *ACM Transactions on Graphics*, page 1–12, Nov 2016.
- [12] Glenn E Healey and Raghava Kondepudy. Radiometric ccd camera calibration and noise estimation. *IEEE Transactions on Pattern Analysis and Machine Intelligence*, 16(3):267–276, 1994.
- [13] Bernhard Hill, Th Roger, and Friedrich Wilhelm Vorhagen. Comparative analysis of the quantization of color spaces on the basis of the cielab color-difference formula. *ACM Transactions on Graphics (TOG)*, 16(2):109–154, 1997.
- [14] Berthold KP Horn and Robert W Sjoberg. Calculating the reflectance map. *Applied optics*, 18(11):1770–1779, 1979.
- [15] A. Huggett, C. Silsby, S. Cami, and J. Beck. A dual-conversion-gain video sensor with dewarping and overlay on a single chip. In *IEEE International Solid-state Circuits Conference-digest of Technical Papers*, 2009.
- [16] Nima Khademi Kalantari, Ravi Ramamoorthi, et al. Deep high dynamic range imaging of dynamic scenes. *ACM Trans. Graph.*, 36(4):144–1, 2017.
- [17] Diederik P. Kingma and Jimmy Ba. Adam: A method for stochastic optimization. *arXiv: Learning*, 2014.
- [18] S. Lee, G. H. An, and S. J. Kang. Deep chain hdri: Reconstructing a high dynamic range image from a single low dynamic range image, 2018.
- [19] Chih-Hung Liang, Yu-An Chen, Yueh-Cheng Liu, and WinstonH. Hsu. Raw image deblurring. *arXiv: Image and Video Processing,arXiv: Image and Video Processing*, Dec 2020.
- [20] Yihao Liu, Jingwen He, Xiangyu Chen, Zhengwen Zhang, Hengyuan Zhao, Chao Dong, and Yu Qiao. Very lightweight photo retouching network with conditional sequential modulation. *IEEE Transactions on Multimedia,IEEE Transactions on Multimedia*, Apr 2021.
- [21] Zhen Liu, Wenjie Lin, Xinpeng Li, Qing Rao, Ting Jiang, Mingyan Han, Haoqiang Fan, Jian Sun, and Shuaicheng Liu. Adnet: Attention-guided deformable convolutional network for high dynamic range imaging. In *Proceedings of the IEEE/CVF Conference on Computer Vision and Pattern Recognition*, pages 463–470, 2021.
- [22] Zhen Liu, Yinglong Wang, Bing Zeng, and Shuaicheng Liu. Ghost-free high dynamic range imaging with context-aware transformer. In *Computer Vision–ECCV 2022: 17th European Conference, Tel Aviv, Israel, October 23–27, 2022, Proceedings, Part XIX*, pages 344–360. Springer, 2022.

[23] Ymir Mäkinen, Lucio Azzari, and Alessandro Foi. Collaborative filtering of correlated noise: Exact transform-domain variance for improved shrinkage and patch matching. *IEEE Transactions on Image Processing*, 29:8339–8354, 2020.

[24] J. S. McElvain, W. C. Gish, J. R. Miller, G. J. Ward, and R. Atkins. Auto exposure of spatially-multiplexed-exposure high-dynamic-range image sensors, 2021.

[25] S. K. Nayar. High dynamic range imaging: spatially varying pixel exposures. In *IEEE Conference on Computer Vision & Pattern Recognition Cvpr*, 2002.

[26] Nima, Khademi, Kalantari, Ravi, and Ramamoorthi. Deep hdr video from sequences with alternating exposures. *Computer graphics forum : journal of the European Association for Computer Graphics*, 38(2):193–205, 2019.

[27] Y. Niu, J. Wu, W. Liu, W. Guo, and Rwh Lau. Hdr-gan: Hdr image reconstruction from multi-exposed ldr images with large motions. *arXiv e-prints*, 2020.

[28] Niki Parmar, Ashish Vaswani, Jakob Uszkoreit, Lukasz Kaiser, Noam Shazeer, Alexander Ku, and Dustin Tran. Image transformer. In *International conference on machine learning*, pages 4055–4064. PMLR, 2018.

[29] K Ram Prabhakar, Susmit Agrawal, Durgesh Kumar Singh, Balraj Ashwath, and R Venkatesh Babu. Towards practical and efficient high-resolution hdr deghosting with cnn. In *Computer Vision–ECCV 2020: 16th European Conference, Glasgow, UK, August 23–28, 2020, Proceedings, Part XXI 16*, pages 497–513. Springer, 2020.

[30] Guocheng Qian, Yuanhao Wang, Jinjin Gu, Chao Dong, Wolfgang Heidrich, Bernard Ghanem, and Jimmy S Ren. Rethinking learning-based demosaicing, denoising, and super-resolution pipeline. In *2022 IEEE International Conference on Computational Photography (ICCP)*, pages 1–12. IEEE, 2022.

[31] Mushfiqur Rouf, Rafal Mantiuk, Wolfgang Heidrich, Matthew Trentacoste, and Cheryl Lau. Glare encoding of high dynamic range images. *Computer Vision and Pattern Recognition*, 2011.

[32] Victor Sanh, Lysandre Debut, Julien Chaumond, and Thomas Wolf. Distilbert, a distilled version of bert: smaller, faster, cheaper and lighter. *arXiv preprint arXiv:1910.01108*, 2019.

[33] Q. Sun, E. Tseng, Q. Fu, W. Heidrich, and F. Heide. Learning rank-1 diffractive optics for single-shot high dynamic range imaging. In *cvpr*, 2020.

[34] Yuzhi Wang, Haibin Huang, Qin Xu, Jiaming Liu, Yiqun Liu, and Jue Wang. Practical deep raw image denoising on mobile devices. In *Computer Vision–ECCV 2020: 16th European Conference, Glasgow, UK, August 23–28, 2020, Proceedings, Part VI*, pages 1–16. Springer, 2020.

[35] Kaixuan Wei, Ying Fu, Jiaolong Yang, and Hua Huang. A physics-based noise formation model for extreme low-light raw denoising. In *Proceedings of the IEEE/CVF Conference on Computer Vision and Pattern Recognition*, pages 2758–2767, 2020.

[36] Shangzhe Wu, Jiarui Xu, Yu-Wing Tai, and Chi-Keung Tang. Deep high dynamic range imaging with large foreground motions. In *Proceedings of the European Conference on Computer Vision (ECCV)*, pages 117–132, 2018.

[37] Q. Yan, D. Gong, Q. Shi, Avd Hengel, and Y. Zhang. Attention-guided network for ghost-free high dynamic range imaging. In *2019 IEEE/CVF Conference on Computer Vision and Pattern Recognition (CVPR)*, 2019.

[38] Q. Yan, D. Gong, P. Zhang, Q. Shi, J. Sun, I. Reid, and Y. Zhang. Multi-scale dense networks for deep high dynamic range imaging. In *Workshop on Applications of Computer Vision*, 2019.

[39] Q. Yan, L. Zhang, Y. Liu, Y. Zhu, J. Sun, Q. Shi, and Y. Zhang. Deep hdr imaging via a non-local network. *IEEE Transactions on Image Processing*, 29:4308–4322, 2020.

[40] Qingsen Yan, Lei Zhang, Yu Liu, Yu Zhu, Jinqiu Sun, Qin-feng Shi, and Yanning Zhang. Deep hdr imaging via a non-local network. *IEEE Transactions on Image Processing*, 29:4308–4322, 2020.

[41] Z. Yan and J. Fang. The low-frequency noise of hgcdte sensor with overlap structure. In *Noise and Information in Nanoelectronics, Sensors, and Standards II*, 2004.

[42] Huanjing Yue, Cong Cao, Lei Liao, Ronghe Chu, and Jingyu Yang. Supervised raw video denoising with a benchmark dataset on dynamic scenes. In *Proceedings of the IEEE/CVF conference on computer vision and pattern recognition*, pages 2301–2310, 2020.

[43] Huanjing Yue, Yijia Cheng, Yan Mao, Cong Cao, and Jingyu Yang. Recaptured screen image demoiréing in raw domain. *IEEE Transactions on Multimedia*, page 1–12, Jan 2022.

[44] Xuaner Zhang, Qifeng Chen, Ren Ng, and Vladlen Koltun. Zoom to learn, learn to zoom. In *Proceedings of the IEEE/CVF Conference on Computer Vision and Pattern Recognition*, pages 3762–3770, 2019.

[45] Xuemei Zhang, Brian A Wandell, et al. A spatial extension of cielab for digital color image reproduction. In *SID international symposium digest of technical papers*, volume 27, pages 731–734. Citeseer, 1996.

[46] Xindong Zhang, Hui Zeng, and Lei Zhang. Edge-oriented convolution block for real-time super resolution on mobile devices. In *Proceedings of the 29th ACM International Conference on Multimedia*, pages 4034–4043, 2021.

[47] Yi Zhang, Hongwei Qin, Xiaogang Wang, and Hongsheng Li. Rethinking noise synthesis and modeling in raw denoising. In *Proceedings of the IEEE/CVF International Conference on Computer Vision*, pages 4593–4601, 2021.